Desalination and Water Treatment
www.deswater.com
doi: 10.5004/dwt.2019.24688

169 (2019) 59–71
November

Novel formulations for scalable multilayer nanoporous graphene-based membranes for use in efficient water detoxification revisited

Sanju Gupta*, Alex Henson§, Brendan Evans§

Department of Physics and Astronomy, Western Kentucky University, 1906 College Heights Blvd. Bowling Green, KY 42101, USA, emails: sanju.gupta@wku.edu (S. Gupta), alex.henson836@topper.wku.edu (A. Henson), brendan.evans054@topper.wku.edu (B. Evans)

Received 27 January 2019; Accepted 9 July 2019

ABSTRACT

In this work, we have developed multilayer nanoporous graphene oxide-based membranes by (1) taking advantage of nematic liquid crystalline phase of graphene oxide (GO) and alignment of pores through shear forces (SA GO) and (2) holey graphene (hG) with extremely controlled narrow pore size distribution via catalytic metal oxidation, for the efficient transport of water and rejection of undesired solute ions, as potential successor of reverse osmosis nanofiltration membranes. The membranes performance was evaluated by measuring flux (permeability) and rejection (retention and adsorption) with applied pressure using a dead-end filtration cell investigating steady-state permeation properties. These ordered, continuous SA GO and hG membranes (~140 ± 20 nm thick) demonstrated faster water transport (higher permeability; ~70 ± 12 L m^{-2} h^{-1} bar^{-1}), higher retention for charged and uncharged organic probe molecules (>95%) with hydrated radii >5 Å and modest (~40%) to high (~70%) rejection of mono- and divalent ion salts. The superior flux and efficient transports are attributed to the formation of in-plane organized, molecule-hugging cylindrical (slit-like) and spherical (pore-like) nanochannels with optimum interlayer distance, low friction and large slip length of water following pore-flow model. The ion rejection mechanism from these primarily negatively charged membranes reveal that physical sieving and electrostatic interactions dominate the filtration process. We also presented the results with extremely cost-effective use of xylem plant as a natural filtration medium for economical disadvantaged regions and countries where potable freshwater is limited or lacking. These findings demonstrate a facile scalable method to obtain *G*-based membranes with reasonable good stability, adjustable thickness and tunable interlayer spacing, thereby eliminating problems typically caused by aggregation limiting practical use of functional moieties.

Keywords: Graphene oxide; Shear alignment; Holey graphene; Membranes; High permeability; Ion selectivity

1. Introduction

Water is one of the planet's most precious resources and life's most basic and indispensable component. The reverse osmosis (RO) filtration in water purification is increasingly used to produce potable freshwater for growing world population, with currently greater than 50% of desalination plants worldwide using RO technology [1–3]. RO is a process by which pre-filtered seawater is forced through a series of semipermeable membranes under a pressure that is greater than the osmotic pressure, producing potable water by removing ions, molecules, biomolecules and larger particles [3]; it requires approximately 3 kW h^{-1} of energy per kg to produce 1 m^3 of drinking water. Dwindling water resources with global increase in cleaning water consumption requiring lot of energy forces to re-consider advanced

* Corresponding author.

§ Co-authors are undergraduate students who contributed to this work equally.

and novel conceptualization of water filtration technologies, which can provide safe supply in a faster and more energy-efficient, environmentally sustainable way [4]. Advances in the strategic design and synthesis of water filtration membranes with significantly improved retention, flux and cost-effectiveness will have tremendous impacts [5]. Current membranes based on conventional polymers (e.g. polyamide; PA) and ceramics used in molecular separation, sensing, biomedical and water purification technologies have salient advantages. However, these membranes suffer from limitations that call out the development for the conception of novel membranes that offer high permeability (water flux), ion differentiation (selectivity) and structurally stable, scalable, reproducible, cost-effective as well as energy efficient. Graphene–atomic thin two-dimensional honeycomb sp^2 bonded carbon lattice–is an exciting and potential game changing multifunctional nanomaterial, that possesses a combination of strong mechanical properties, extremely large surface area, chemical inertness and imperviousness to atoms even as small as Helium [4,6]. These nanoscale materials have shown potential in a variety of applications including water desalination and purification, electrochemical energy systems (supercapacitors and Li-ion batteries) [7–9], electrocatalytical enzyme-free biosensors [10,11], and proton conductors [12]. The concept of graphene-based membranes was first realized by molecular dynamic (MD) simulations where nanopores were simulated on the surface or basal plane of high strength graphene monolayers to allow water to permeate while selectively rejecting other undesired substances proficiently [13]. Controlled by pore size and functional groups on the nanopore edge, one could make monolayer graphene useful for water filtration/desalination with higher permeability than those of current RO membranes, was elucidated. Recent experiments of graphene-based membranes prepared from monolayer graphene with arrays of nanosize holes provide ultrathin, ultrafast transport, high flux, energy-efficient, precise molecular sieving of gas and solvated molecules demonstrate great promise [6,14–18]. Despite of MD simulations and various experimental demonstrations and efforts, significant technical challenges exist as they suffer from manufacturing benefits that require expensive equipment and employ laborious methods in creating membranes with organized nanopores for practical purposes such as scalability, reproducibility and mechanical robustness due to thinness. Other potential two-dimensional layered materials suggested for similar applications are molybdenum disulfide (MoS_2) monolayers [19] and hexagonal boron nitride (h-BN) [20]. Therefore, developing few- and multilayer nanoporous graphene (mNPG) membranes present viable and energy–efficient alternatives for the RO desalination process [7,15,21].

Graphene oxide (GO) particularly, which is a pseudo-two-dimensional material with strong in-plane covalent bonding and weak interlayer contacts made by hydrogen bonds between intercalated water molecules, is useful for their easy processability [22]. The carbons in GO nanoscale flakes contain basal embedded hydroxyl (–OH) and carbonyl (–CO) functional groups as well as carboxyl (–COOH) groups situated at the edge sites of the sheets [23]. As a result, these surface functionalized graphene namely GO offers extraordinary potential for making functional systems and composites with high chemical stability and mechanical robustness, strong hydrophilicity, excellent antifouling and antibacterial properties, all of which are promising in water detoxification processes [24]. Several other advantages of GO-based multilayer membrane technologies include cost-effectiveness, scalability due to facile syntheses, safety, environmentally friendliness and easy recyclability. Likewise, holey graphene (hG)–closed-edge nanopore contained in graphene nanosheet–prepared from thermally reduced rGO in bulk using different methods (helium ion and electron beam drilling, defect-selective electron recoil sputtering, focused ion beam direct writing, metal catalyzed oxidation process) for precise control of nanopore size distribution [25–27]. In fact, edge sites are equally emerging for functionalization with single-ion biological channels or biomolecules for preparing biologically-inspired and biomimetic membranes, sequencing of DNA, single-molecule detection besides water detoxification [28–30]. In spite of many reports on multilayered GO-based membranes [7,15,31] and graphene with arrayed holes [23,24,32], this work revisits on the strategic production of next-generation large-area mNPG oxide and hG membranes [24].

To achieve mNPG membranes with high water permeability and salt rejection rate, we employed the following design guidelines based on modeling and simulations: (1) Both pore alignment and layer separation could be precisely controlled, a mNPG membrane with the smallest possible layer separation and fully aligned pores would represent the most promising choice. (2) It would be preferable to have sufficiently large layer separation to avoid fully impeding water passage across misaligned pores. Although large pore offsets would lead to a lower flux per membrane area, salt rejection could be enhanced. Additional NPG layers could be also used to further increase salt rejection; (3) Pores offset can be controlled experimentally and it is suggestive that a membrane with fully aligned pores is desirable. Although a large layer separation may result in lower salt rejection, more layers could then be superimposed to achieve the requisite salt rejection; and finally, (4) when neither pore alignment nor layer separation is controlled, having NPG membrane with the greatest pore density is recommended to enhance the likelihood of having aligned pores such as in this study. Furthermore, a larger pore density per unit area results in a higher net water flux per membrane area. Specifically, we report on the preparation of shear-aligned (SA) GO membranes driven by liquid crystalline phase transition of GO [33] and controlled metal catalyzed hG membranes using facile methods on microporous Nylon support membrane [23,30]. They are expected to have optimized functional pore-pore alignment (organized) and interlayer distance in concurrent with mechanical robustness and chemical stability needed during pressure driven RO process. The performance evaluation in terms of permeability (or flux) and retention is carried out to elucidate the roles of several key parameters such as pore size, shape (slit-like and hole-like), alignment (random vs. organized), pore edge and membrane surface functional chemistry. The various results were discussed while addressing the following questions: Are the SA GO and hG membranes' performance reproducible? Can we affect the quality of multilayer SA GO films by varying

the conditions of their deposition and post-processing such as thermal reduction? How the nanopore size, shape, alignment affect the filtration and desalination performance? We strongly believe this work will also open up new innovations for nanoporous graphene-based membranes with other significant value propositions those are less prone to fouling, resistant to scaling, stable to chlorine and extreme pH, by designing nanocomposite thin film membranes with interfacial polymerization, for instance, among other strategies.

2. Experimental setup

2.1. Materials and methods

2.1.1. Synthesis of GO dispersions and hG

GO was synthesized using modified Hummers' method as described [34–36]. According to the work reported in literature [7], an additional graphite oxidation procedure was needed, otherwise, incompletely oxidized graphite (core)/GO (shell) microparticles were observed in the final product. Briefly, natural graphite powder (4 g, Flake Graphite, Graphene Supermarket, TX), concentrated sulfuric acid H_2SO_4 (25 mL) containing $KMnO_4$ (5 g) and $NaNO_3$ (5 g) (Sigma-Aldrich, St. Louis, MO) as strong oxidizing agents were used for the synthesis. The synthesized GO product is re-suspended in water to a brown dispersion, which is subjected to dialysis to remove residual metal ions and acids. The purified GO dispersion is sonicated by centrifugation (3,000 rpm and 10 min) for exfoliation in RO water for 2.5 h, followed by centrifugation to remove the aggregated and un-exfoliated GO. The average lateral size of the GO nanosheets were determined using a scanning electron microscopy (SEM) (Model JSM-6510LV, MA) estimated to be ~1.5 ± 0.4 mm. A UV–Vis–NIR spectrophotometer (Perkin-Elmer 1050) in a range of 200–700 nm was used to determine the GO concentration via measuring the absorbance at 230 nm (not shown). Various concentrations of GO dispersions were prepared using a superabsorbent polymer (cross-linked polyacrylate based hydrophilic hydrogel beads, Alibaba, China). For example, within ~2.5 h, a 12.5 ml GO dispersion with a concentration of 10 mg mL^{-1} within ~2.5 h was obtained from a 500 ml suspension of 0.25 mg mL^{-1} GO where we used 11.5 g of hydrogel beads. This process is repeated to produce concentration GO of 14, 16 and 20 mg mL^{-1} viscous colloidal dispersions [29,31]. To avoid possible concentration around the beads and to speed up the absorbent process the container was mildly agitated by a magnetic stirrer. After the hydrogel beads were saturated with water, they were removed from the concentrated solution, cleaned with RO water. The GO deposits adhering to the surface of the saturated beads were also removed by washing them with RO water. The saturated hydrogel beads could be reused after drying them at 50°C overnight or leave them for drying in the air for 24–48 h. Fig. 1a summarizes the procedural steps. The as-prepared GO samples resulting in ratio of C:O (2:1) were then characterized with SEM and transmission electron microscopy (TEM) (Model 1400 Plus, OR).

The hG (see Fig. 1b) [24] preparation involves multistep process and it begins by creating mixture of thermally reduced rGO and silver acetate of two molar concentrations 1% (9% silver acetate and 91% rGO wt.%) and 10% (47% silver acetate and 53% rGO wt.%) with both mixtures being 100 mg total. Thermal reduction took place at relatively low temperature of 180°C for 2 h in Ar atmosphere yielding C:O ratio of 8:1 measured through X-ray energy dispersive spectroscopy (Model JSM-6510LV, MA). These two mixtures were mechanically grinded for homogenization with a mortar and pestle for 30–60 min. The solid mixtures were then transferred to an appropriate container (e.g. Al pan or ceramic boat) and heated in Ar gas atmosphere in a tube furnace (Lindberg blue, Ar gas flow rate ~80–100 cm^3 min^{-1}) to 350°C over 1 h, held isothermally for 3 h and cooled to room temperature. The temperature of the furnace was increased at 10°C min^{-1}. The cooled product was then collected as the $(Ag\text{-}rGO)_1$ and $(Ag\text{-}rGO)_{10}$ samples, were the subscript refers to Ag-to-C molar ratio in percentage. For metallized catalytic oxidation, these vessels were moved into an open-ended tube furnace or an air oven to a given temperature of 300°C over 1.5 h and held isothermally for 3 h to perform metal catalytic oxidation. The heating was performed to create the functionalized holes as nanopores in graphene sheets to enhance filtration properties. For catalysts removal, in a typical reaction, these air-oxidized Ag-rGO samples (50 mg) were refluxed in diluted nitric acid (HNO_3, 2.3 M, 30 ml) for 2 h to remove silver particles following 30 min to cool. These solutions were then transferred into falcon tubes for centrifugation at 5,000 rpm for 10 min and the supernatant was discarded. The solid then repeatedly washed with water from 8 to 10 times in re-dispersion-centrifugation cycles until the supernatant become neutral (pH > 6.2). The solid was then dried either at 70°C in vacuum or at room temperature under a constant Ar flow to obtain the final hG_1 and hG_{10} products. Typically, the yield was approximately 70%–80% for both the hG_1 and hG_{10} samples (air oxidation at 300°C for 3 h).

2.1.2. SA GO and hG membranes preparation

To evaluate the optimal conditions required for production of a continuous GO film, a simple lab-scale doctor blade (MTI Corporation, USA) was used for various GO concentrations. The doctor blade had a relatively finer rectangular outlet formed between the blade and the substrate, through which the movable blade spreads the nematic phase GO dispersions on the substrates (Fig. 1c). Fig. 1c also shows the photographs of the as-prepared multilayer nanoporous membrane discs namely, GO_{bead}, hG_1 and hG_{10} clearly revealing far more uniformity and denser without pinholes and patched as opposed to vacuum filtered membrane GO_{vac}. The doctor blade gap size was ~2 mm and the casting speed was ~0.5 cm s^{-1}. To prepare GO film, 0.25 ml of GO dispersion was spread over a porous Nylon-66 membrane (pore size 0.2 mm, 4.7 cm diameter, Sterlitech, USA). A syringe pump was used to precisely control the movement of the doctor blade. Subsequently, the resultant liquid films were dried overnight under ambient condition. To prepare both types of hG membranes, we used Nylon-66 support membrane and a vacuum filtration pump (KNF pump) from the purified solutions. We also prepared vacuum filtered GO membranes by using a 5.0 and 7.5 mg ml^{-1} GO solution (from same stock of GO dispersion) and filtered it through the same porous Nylon-66 support (pore size 0.2 mm, 47 mm diameter,

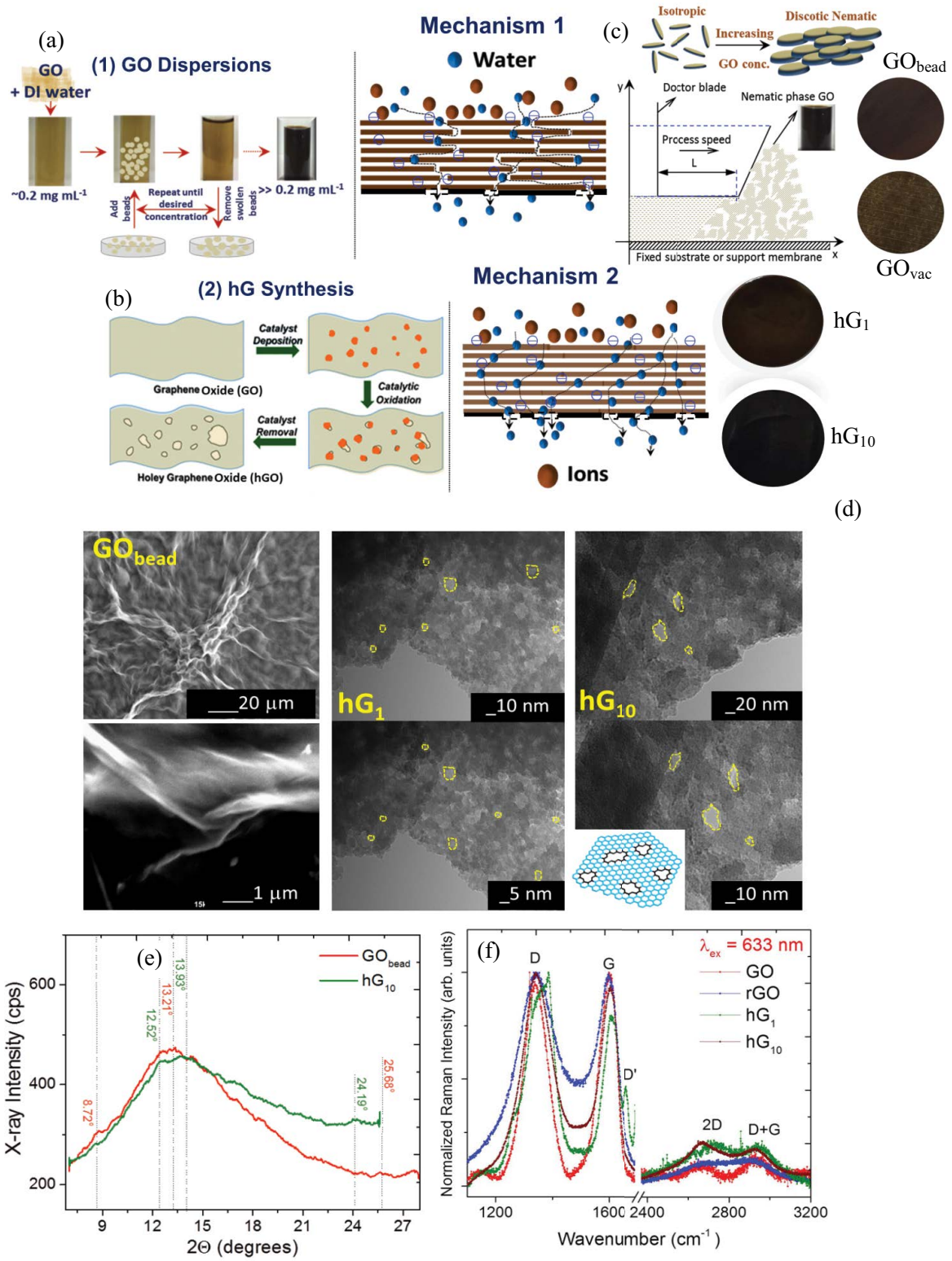

Fig. 1. (a) Procedure for concentration GO dispersions by adding polymer hydrogel beads. (b) Schematic of the scalable synthesis of hG sheets via catalytic metal oxidation in air. (c) Shear-aligned processing of nematic GO film. Also, shown as-prepared GO_{bead}, GO_{vac}, hG_1 and hG_{10} membrane discs revealing uniformity without pinholes. (d) SEM images of GO films demonstrate continuity and conformity of SA membranes over Nylon 66 membrane support and TEM images of hG_1 and hG_{10} showing almost uniform pore size distribution. A cartoon of holey graphene nanosheet is included in inset of hG_{10} image. (e) X-ray diffraction of SA GO and hG_{10} films (e) Micro-Raman spectra of SA GO_{film}, rGO, hG_1 and hG_{10} films showing prominent first-order (*D*, *G*) and second-order (2*D*, *D* + *G*) bands besides *D*′ band for hG film.

Sterlitech, USA) for comparison with SA GO membranes. Different thicknesses of membrane can be made by changing the volume of the GO solution.

2.1.3. Design of xylem plant as natural wood filtration medium

For creating wood filter [37], branches were excised from white pine tree (identified as *Pinus strobus* based on the 5-fold cone needles grouping) growing on a private property on north side of Kentucky and placed in RO drinking water. Wood sections after peeling off the bark with cambium of different length and 1 cm diameter giving various aspect (L/D) ratio (0.833, 1.67, 2.50) were cut and inserted at the end of 1 cm internal diameter tygon tubing, sealed with quick fix epoxy, secured with hose clamps and allowed to cure for 30–40 min before conducting flow rate/filtration experiments (see Fig. 1).

2.1.4. Microstructure characterization

All of the samples were characterized using a range of complimentary techniques to reveal surface morphology, microstructure and lattice vibration properties. SEM images were taken while operating at a primary electron acceleration voltage (V_{acc}) of 10–20 kV at constant current 45 μA in secondary electron imaging mode with a LaB_6 filament. For TEM, images were taken using a JEOL (Tokyo, Japan) instrument operating in cryo-EM and SAED modes at 100–120 kV and 1 nA from LaB_6 gun with a Be specimen holder, a Gresham SiLi detector and with AMT 8 Mpixel cooled camera. TEM measurements provided nanoscale morphology and structure that help to determine interplanar spacing. The X-ray diffraction (XRD) was measured using a Bruker (Billerica, MA) (Model D2 PHASER) diffractometer with Cu K_a line generated at 40 kV and 30 mA at a scan rate of 0.2° min^{-1} and a step size of 0.02° in the range of 2q = 5°–70° for SA GO and hG membranes. The XRD and TEM samples were prepared by etching the Nylon 66 substrates with concentrated HCl acid (Sigma-Aldrich, St. Louis, MO) and transferring the free-standing SA GO and hG films on glass slides or TEM grids. Raman spectra were measured using a micro-Raman spectrometer (Model InVia Renishaw plc, Hoffman Estates, IL, USA) equipped with a laser providing excitation wavelength 633 nm. The scattered light from the sample is collected in backscattering geometry transmitted and detected by CCD camera. An objective lens of 50*x* was used providing a spot size of ~1–2 mm and the laser power on the sample is maintained between <0.1–0.5 mW (1% or 5%) to avoid local heating effects. Raman spectra ranged from 120–3,200 cm^{-1} samples for nitrogenated samples from 1,100 to 3,200 cm^{-1} for non-nitrogenated aerogel samples with spectral resolution of 1 cm^{-1}.

Xylem structure was visualized using SEM. Samples were sliced and coated with 10 nm thick gold before imaging for better visualization.

2.1.5. Nanofiltration performance of the membranes and wood filter

The SA GO and hG membranes were cut into the required size (43 mm diameter) of cell during nanofiltration tests. To increase the water stability of the SA GO and vacuum membranes, they were exposed to 30 ml of hydrazine hydrate vapor (90%, Sigma-Aldrich, St. Louis, MO) for 10 min by placing in a hermetically sealed vessel containing the GO membrane onto a hot-plate at 60°C causing partial chemical reduction. We also soaked these SA GO membranes in 0.2 M NaCl and KCl for tuning interlayer spacing and nanochannel length via cationic intercalant control. The water permeability and salt ion retention capabilities of the membranes were examined using a commercial bench-scale dead-end stirred cell-filtration unit (Sterlitech, Model UHP43, Kent, WA). The effective membrane area was ~14.5 cm^2 and all the experiments were performed at ambient conditions (25°C) with pressure applied from 0.5 to 5 bar (60 psi or 413.7 kPa). Pressure was supplied using a nitrogen tank with a pressure regulator for all the experiments. The permeability (χ) of the membranes (with units L h^{-1} m^{-2} bar^{-1}) for pure water, salt water and water/organic probe dye molecule solutions was determined after a constant flux was obtained, typically after 1 h of permeation, and calculated as:

$$\chi = \frac{V_p}{t \cdot A \cdot \Delta P} \tag{1}$$

where V_p is the permeate volume, t is the permeation time, A is the membrane active area and DP is the applied pressure of nitrogen. Prior to evaluation for retention performance of the membranes, the stirred cell was filled with 10 mg L^{-1} of the test solutions. To diminish the role of adsorption, the membranes were pre-saturated by filtering ~20 ml of the test solution and then, to remove any solute adhered to the membrane surfaces, the membranes were thoroughly washed with acetone followed by RO water (typically 50 ml of the solvent was added to the filtration cell and left stirring at 500 rpm for 5 min). It is noteworthy that the cleaning process removed most of the probe molecules adhering to membrane surface and almost 100% recovery of membrane was observed. The retention performance of the membranes were evaluated by filling the cell with 40 ml of solution followed by applying pressure and allowing 10 ml to permeate through it. The 10 ml, which permeated through the membrane were collected and analyzed. All tests were repeated five times for reproducible results. For accurate estimation of the concentration of the probe dye molecules in the retentate stream, we rinsed all the components which were in contact with the retentate solution in the filtration cell, such as, the stirring apparatus, interior walls of the cell and the top surface of the membranes with 100 ml of RO water multiple times and accounted for during calculation of the retentate concentration.

The salt retention performance of the SA GO and hG membranes was examined by evaluating the retention of the selected monovalent and divalent salts, NaCl, KCl, $MgCl_2$, $CaCl_2$, Na_2SO_4, K_2SO_4, $MgSO_4$ and $CaSO_4$, with a concentration of 0.5 g L^{-1}. To minimize the concentration polarization effect on the retention performance, the feed solution was occasionally stirred at 500 rpm during the filtration. We begin the tests by recording the permeability of the membranes for RO water until a stable condition was achieved (typically 1 h). Subsequently, RO water is replaced by 40 ml of the salt solution. The salt retention performance

of the membranes was evaluated by filtering 5–10 ml of the initial feed of 40 mL. Before every experiment, the membrane was cleaned by filtering RO water through them until the permeability became stable and evidence of salts were observed typically 1–2. The retention performances of the membranes for the salts were calculated using the equation:

$$R(\%) = \frac{C_f - C_p}{C_f} \times 100(\%) \quad (2)$$

where C_f is feed and C_p is permeate concentration, respectively. The concentrations of the salts were also measured by an ion conductivity meter (Cole-Palmer, Vernon Hills, IL, Model Oakton CON 450 Meter). Likewise, adsorption of probe dyes is calculated using:

$$\text{Ads.}(\%) = \frac{V_f C_f - (V_r C_r + V_p C_p)}{V_f C_f} \times 100(\%) \quad (3)$$

where C_p is the concentration of permeate and V_f, V_r and V_p refers to the volume of feed, retentate and permeate, respectively. The C_f for all the molecular dyes used was 10 mM. Once all filtration was complete we kept it in a ~1–2 ml amount of filtered R6G (Rhodamine 6G), MB (Methylene Blue) and MV (Methyl Viologen) to determine the concentration of permeate and retentate by analyzing permeate through UV-Vis absorption spectroscopy (Perkin-Elmer 1050, spectrophotometer, Waltham, MA). As for wood filters, they were flushed with 20 mL of RO water before experiments. Approximately 15 mL of deionized water or solution was placed in the tube. The filtrate was collected in glass vials. Care was taken to avoid drying of the filter and they were therefore soaked in RO water before and after use.

3. Results and discussion

3.1. Liquid crystalline phases of GO production and SA membrane

The liquid crystalline phase of anisotropic GO nanoflakes (lateral size to thickness ratio ~1 k) suspended in water as stable colloidal suspension is produced by a unique sample concentration method, based on the superabsorbent polymeric hydrogel beads [38], unlike by application of heat or using vacuum [39,40]. They swell with water by absorbing small particles and water molecules within the beads, but larger particles are excluded and they are concentrated in the remaining un-absorbed water. In fact, similar approach is adopted for concentrating bacteria and other micro-organisms while detecting and quantifying pathogens in water while addressing water-borne diseases [41]. In general, as the concentration of GO dispersion increases, the GO nanoflakes undergo a structural phase transition , that is, from an isotropic dispersion to a biphasic system followed by full discotic nematic liquid crystal phase. The liquid crystal gel-like mesomorphic system displays a defect-free uniform director alignment over hundreds of micrometers. The duration for this process depends upon the initial concentration, the desired concentration and amount of hydrogels beads used. Fig. 1c shows the ~30 mg ml^{-1} concentrated GO dispersion [29,31].

The most important goal of this work is to fabricate scalable and membranes with reproducible performance taking advantage of this discotic nematic liquid crystalline phase of GO dispersion, by shear-induced alignment, going beyond the high solid contents of GO to produce continuous films. In our work, we observed an isotropic (0.25 mg ml^{-1}) to nematic phase transition at 7.5 mg ml^{-1}, biphasic at 16 mg ml^{-1} and complete nematic phases at ^{3}20 mg ml^{-1} or beyond. It is known that nematic ordered fluid phases of GO have non-Newtonian flow characteristics [29,42], which are used to produce large-area films by use of shear forces applied through either doctor blading (a rigid blade typically used in liquid thin film processing for polymeric films) or dip coating [43]. While the size of membrane is governed by the shearing apparatus, we produced continuous films of area ~20 cm^2 using a lab-scale doctor blade. The viscosity of the fluid is an important material parameter imposed during shear stress producing homogeneous films over large areas known as shear-thinning phenomena despite high viscosity. Fig. 1c shows the shearing process and the corresponding photographs of the shear-alignment (SA GO) membranes on porous Nylon-66 substrates (namely, GO_{bead}) besides SEM (Fig. 1d) displaying surface uniformity. To stabilize the membranes, we partially reduced the GO membranes by exposure to hydrazine hydrate vapor for 10 min. followed by soaking in cationic (NaCl and KCl) solution for cation-controlled interlayer spacing.

3.2. hG membrane

Figs. 1b and d shows photograph of hG membranes showing uniformity and TEM images of both the hG_1 and hG_{10} membranes, respectively. The nanocrystalline domains and point defects on the graphene basal planes react with oxygen in the presence of metal catalyst leaving holes upon catalytic oxidation by etching away carbon atoms on the sheets primarily at the location of the metal catalyst. The electron microscopy shows the nanopore size distribution controlled by the amount of Ag metal catalyst content with respect to carbon, higher amount led to larger average size of Ag nanoparticles. It resulted in overall optimally sized holes adopted by the size of the nanopores in hG membranes. The hole or nanopore size for hG_{10} ranged from 10–20 nm as compared with hG_1 which was ~5 nm in average diameter. Typically, the hG_1 samples have a lower degree of oxidation with the same temperature treatment making its hole size close to Ag-graphene contact area (smaller than the average diameter of Ag nanoparticles) in contrast to hG_{10} sample which has higher contact area as well as lower oxidation threshold that have holes with diameters closer or sometimes larger due to hole merging than the original size of Ag nanoparticles. Interestingly, the edge planes around the holes of hG samples appeared to be relatively smoother. Moreover, nitric acid treatment tends to introduce oxygen-containing groups such as carboxylic acid (–COOH) to sp^2-bonded C (sp^{2}C) systems. The micro-Raman spectra are XRD shown in Fig. 1e and f, respectively, are consistent with this observation. In particular, there was not significant change in interplanar spacing deduced from peak at 2θ = 13.93° identified as d_{002} and the relative change in intensity of D (1,340 cm^{-1}) and G (1,590 cm^{-1}) bands,

as well as peak positions and band widths, for hG_1 and hG_{10} membranes. The Raman band at 1,620–1,630 cm^{-1} identified as *D′* band is apparent in hG films unlike in GO_{bead} membranes despite some similar observations were made both in XRD and Raman spectra. The *D′* band in highly perforated structures such as hG arises due to many more unsaturated edge carbon sites and substantial defects number density (vacancy plus edge sites). Despite the holey appearance, the rest of the nanosheet structures were still highly crystalline. Therefore, the retained graphitic nature suggests that properties such as electrical conductivity, thermal conductivity and mechanical properties are largely preserved.

3.3. Nanofiltration performance

The water flux (or permeability) and salt ion rejection are the two most important factors defining effectiveness of membranes besides underlying principles of fluid-physics in confined space necessary for describing the performance of mNPG membranes that is now discussed. The SA GO (after soaked in NaCl and KCl for 1 h) and as-synthesized hG_1 and hG_{10} membranes of thickness ~140 ± 20 nm are evaluated by measuring the flow rate in a dead-end filtration cell with RO water, organic probe dye, and various electrolytes to exhibit the most promising trade-offs between flux (permeability) and retention (rejection of unwanted ions) to produce freshwater. The thinness of SA membranes strongly suggests that the shear stress orients the GO mesogens into the plane of the substrate and both of these membranes are suitable for medium scale pressure driven filtration. Fig. 2 summarizes the permeability and flux plots (panels Figs. 2a–c) and flux histograms (panel Fig. 2d) for various salts and dyes. Consequently, the SA GO membranes are also compared with vacuum filtered membranes made from two GO concentrations i.e. 5.0 mg ml^{-1} (GO_5) and 7.5 mg ml^{-1} ($GO_{7.5}$). These membranes were reduced in hydrazine hydrate vapor following similar approach to that of SA GO membrane. The water and salt permeability and retention of three different organic dyes (methyl blue–MB, negatively charged; rhodamine 6G–R6G, electroneutral at pH = 6; and methyl viologen–MV, positively charged) are compared. All of these membranes surface tend to be negatively charged due to the presence of carboxyl (–COOH) or hydroxyl (–OH) groups. While it is not surprising that the retention of organic dyes is improved, water permeability is extremely good due to the optimum stacking ordering of multilayer graphene nanosheets. The SA GO membrane and hG membranes showed water permeability (70 ± 12 L m^{-2}, h^{-1} bar^{-1}) that is approximately eight times larger than those of vacuum filtered membranes (9 ± 5 L m^{-2}, h^{-1} bar^{-1}) at the maximum applied pressure difference. It is apparent that the flux through the membrane increases linearly with increasing applied pressure difference (Fig. 2) following solution-diffusion model [44] or permeability with time.

The modified Hagen-Poiseuille Eq. (4):

$$\text{Flux}(\varnothing) \approx \frac{h^4 \Delta P}{12 L^{12}\, \Delta x} \tag{4}$$

where h is the interplanar distance between graphene sheets (equivalent of channel length vertical to the flow), L is the average lateral length of graphene sheets, η is viscosity of water (0.001 Pa s at 22°C), and Δx the thickness of graphene membranes. Here an approximate explanation of fluid flow through multilayered structures assumes that the flow is through cylindrical (or slit-shaped) or spherical-shaped (circular) pores in which volumetric flow is given by:

$$Q = \frac{h^3 L \Delta \text{p}}{12 \eta l} \tag{5}$$

where the effective channel length $l = L\ \Delta x/h$ (l will be the diameter of circular hole in hG membrane) and an areal density is given by 1 L^{-2}. Therefore, for thickness of ~140–160 nm, this equation yields a flux of 0.5 × 10^{-4} L m^{-2} h^{-1} bar^{-1}, several orders of magnitude smaller than our experimental values. One possible explanation is that the water molecules might go through the defect edge of pores within the graphene sheets of multilayer membranes, leading to smaller L for both circular- and slit-like pores, thereby yielding higher calculated flux for relatively lower applied pressure (Figs. 2a and b). The other possible explanation for the observed response could be the slip flow theory. The basic presumption of Hagen-Poiseuille's equation is laminar flow and no-slip (or liquid flow with zero velocity) at the boundary (membrane-electrolyte) layer [45]. The departure of experimental flux from the classical equation suggests that the velocity of the liquid flow at graphene wall and hG pore edge is not zero. Similar to carbon nanotubes (CNTs) with diameter smaller than 10 nm (few-layer CNTs), a flow enhancement of 10^3–10^4 fold was found for water confined in 1D nanochannels [46]. Such a fast transport of water through CNTs is ascribed due to two reasons: (1) low friction between water and hydrophobic carbon wall and (2) ordered hydrogen bonds formed by the single file or address of water molecules being registered. Likewise, the graphene membranes studied in this work with nanopores also possess frictionless carbon walls and nanocapillaries in 2D form are organized and expected to be mostly aligned. Notably, the oxygen-contained groups on graphene sheets would block water molecules because of strong interaction between them. Thus the graphene regions without or less functional groups are responsible for faster transport of water. This explanation is supported by the fact that neat GO membranes filtered through vacuum showed much less water flux at the same measurement conditions (Fig. 2). Actually, since slip flow theory itself is limited more experiments should be carried out for direct proof to obtain insights into deeper understanding of the fluid transport in confined 2D nanochannels with rectangular (slit) or circular (round) holes.

Now we turn our attention toward the measurements of retention and permeability of several monovalent (NaCl, KCl, Na_2SO_4 and K_2SO_4) and divalent cationic salts ($CaCl_2$, $MgSO_4$ and $MgCl_2$) at concentration of 0.5 g L^{-1} and organic probe dyes of 10 mM concentration with different net charges (see Figs. 2b–d and Figs. 3a–b). The SA GO membrane showed modest retention (between 30%–40%) capability as compared to higher retention (between 50%–70%) from hG membranes (Fig. 3a) with lowest retention (20%–25% of NaCl) for GO vacuum filtered membranes (not shown). The GO interlayer distance is not constant and depends strongly on the GO:H_2O ratio [22]. Therefore this capability

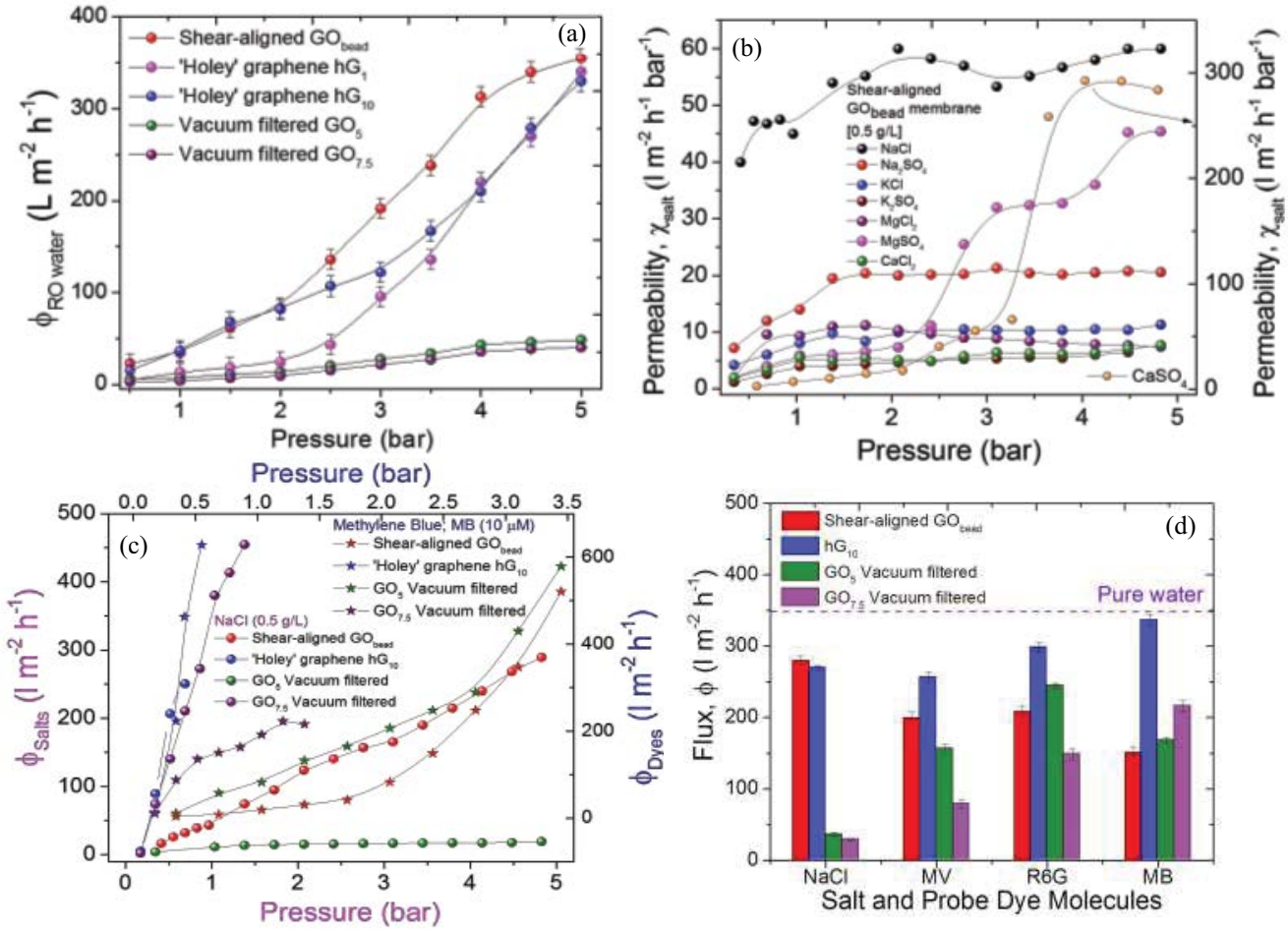

Fig. 2. Filtration performance (a) water flux ((ϕ) vs. applied pressure for various membranes. (b) Permeability (χ) for SA GO membrane for alkali and alkaline salts. (c) Flux (ϕ) of NaCl and methylene blue; MB dye for SA GO membrane and hG_{10} membranes vs. applied pressure. These are also compared with vacuum filtered GO_5 and $GO_{7.5}$ membranes. (d) Flux (ϕ) histograms for NaCl, Rhodamine 6G (R6G), MB, and methyl viologen (MV) dyes at the maximum applied pressure difference. RO water flux is also shown as horizontal dotted line.

is not surprising as the interlayer spacing for SA GO membrane is rather small (~6.3–7.6 Å) as compared with vacuum filtered membranes (~9.2 Å). Also, both (SA GO as well as hG) membranes surface is abundant with various oxygenated functional groups, such as carboxyl, hydroxyl and epoxy, which persisted post mild chemical reduction for stabilization. According to Klinowski et al. [23], the carbons in GO layers contain two domains randomly distributed namely, aromatic regions with unoxidized benzene rings and aliphatic regions with six-membered carbon rings and relative domains size depends on the degree of oxidation. The phenolic hydroxyl groups are acidic and along with carboxyl groups, are responsible for negatively charged surface of GO nanosheets in aqueous suspension. While chemical functionalization of nanopores with hydroxyl groups can enhance permeability, but typically reduces desalination efficiency. The reason being hydroxyl groups provide hydrophilic sites at the edge of pore, which give rise to attraction of water molecules and enhanced flux is due to super denser packing of water molecules inside the pore. It is therefore clear there is a general trend for ion rejection regardless of the type of the pore shape. In other words, ion rejection depends on the pore size or effective membrane area and type of pore plays lesser important role. As shown in Fig. 3a, the retention sequence of salt solutions was $R(NaCl) \cong R(KCl) > R(MgSO_4) > R(CaCl_2) > R(CaSO_4) \cong R(Na_2SO_4)$, comparable to those reported and higher than CNT–based membranes at the concentration used [39], but somewhat lower than those of commercial desalination nanofiltration membranes. There are at least two reasons that can contribute to this effect, first the operation pressure is quite low (<<10 bar) owing to limitation of our filtration device (5.5 bar) and these studies demonstrated that the retention of salts decreases with decreasing applied pressure difference [47]. Secondly, there might be some pores larger than 4 nm and unzipped slit-like pores caused by GO surface oxidation. Therefore, further optimization for both types of multilayer nanoporous membranes will facilitate commercialization.

One of the intriguing observations from Fig. 2b is the permeability of $CaSO_4$ is ~4.5–5 times higher than those of Na_2SO_4 and $MgSO_4$ salts. These measurements were repeated

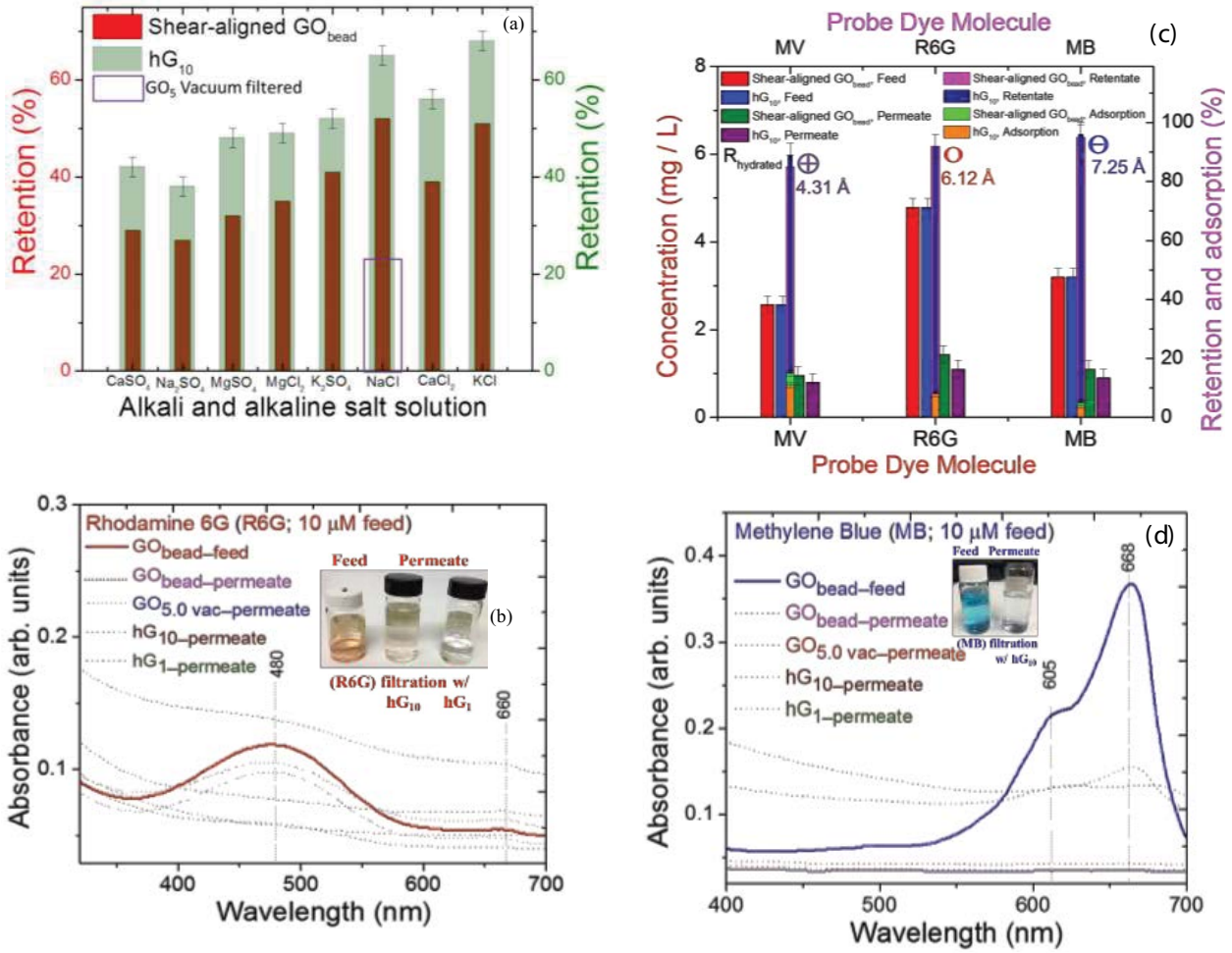

Fig. 3. (a) Various salts retention by SA GO and hG membranes. NaCl retention for GO_5 vacuum filtered membranes is also shown. (b) Retention and corresponding details (concentration and adsorption) of R6G, MB, and MV dyes. The violet, red and blue symbols represent positively, electroneutral and negatively charged organic probe dye molecules, respectively. Error bars in these figures are from four measurements showing the maximum and minimum values. (c, d) Removal of MB and R6G dyes from water by filtration. Images of the solution before (feed) and after (permeate) filtration. The inserts are the UV-Visible absorption spectra of the dye solution before and after filtration from different membranes.

at least four times and here we attempt to provide explanation based on the reported computations helping to gain further insights. The understanding of the ions accumulation on the surfaces with π-electron-rich structures become far more complex due to the cation-π interaction in 1980's [48] as well as hydration or ion solvation effects [49–51]. Basically, the cation-π interaction is the noncovalent interaction between a cation and π-electron-rich carbon-based structure determined using quantum mechanical (DFT and ab initio) methods [50]. While there is clear enrichment of Na^+, Mg^{2+} and Ca^{2+} cations on carbon-based surface, anions (Cl^- and SO_4^{2-}) are also enriched but the hydrated anions-π interaction is much weaker. Moreover, hydrated divalent cations interact strongly than those of monovalent cations, there are subtle differences among divalent ions which require further study. Nevertheless, such singular behavior for Ca^{2+} has been reported earlier while investigating charge transfer dynamics on single-walled CNTs using in situ Raman spectroscopy technique [52].

As for ion transport, it is dominated by flow through large uncovered pores that permit significant flow (pressure driven if pores are <50 nm) and ions can go through the pores without much retardation such that the exclusion of ions can be described using Donnan theory for membrane equilibria. Based on Gibbs-Donnan exclusion theory [39], the Donnan potential at the interphase of feed solution and membranes, these membranes will repel co-ions and consequently retain counterions to keep electroneutrality of the solutions on each side of the membranes. In the exclusion model, the rejection, R, of ionic species can be controlled by the charge density of the membrane by:

$$R = 1 - \frac{C_p}{C_f} = 1 - \left(\frac{|Z_i| C_f}{|Z_i| C_p + X} \right)^{\left|\frac{z_i}{z_j}\right|} \tag{6}$$

where C_f and C_p are concentration of co-ions in the feed and permeate (membrane phase) solutions, X is the membrane

charge density, i and j are the subscripts refer to co- and counter-ions and Z is the ion valence. At a fixed surface charge density (σ), the effective membrane charge density $|X|$ will increase with the decreasing pore diameter, $2r$, as described by a simple scaling relationship [52], $X = \frac{2}{Fr}\sigma$, where F is Faraday constant. In context of Donnan exclusion [19,53,54], the maximum of ~30% rejection of 1 mM NaCl corresponds to a membrane charge density $|X|$ ~0.6 mM. It turns out that the surface charge density for approximately 85% oxidation was measured to be 0.4 per 100 Å^2 by Fendler and co-workers [55]. It implies that, for salts ion rejection more than 30% should result into somewhat lower degree of oxidation of SA GO (as well as hG membranes surface) than 85%, which is consistent with our mild chemical reduction. Computer simulation show that a graphene membrane containing oxygenated groups lined nanopores/nanochannels, such as in our SA GO and hG membranes, can trap Na^+, K^+, Mg^{2+} and Ca^{2+} ions under certain electrochemical conditions and water molecules transport without much retardation. Similar observations have been made in atomically symmetric ultra-narrow nanopores in transition metal dichalcogenides (monolayer molybdenum disulfide, for example) and h-BN [18]. It is established from proton exchange membranes in fuel cells to ion channels in biological membranes, the well-specified control of ionic interactions in confined geometries profoundly influences the transport and selectivity of porous materials. The first principle calculations and density functional theory have revealed that the location of the most stable cation adsorption is where oxide groups and aromatic rings co-exist [50]. The narrow dimensions of the interlayer region or extremely narrow pore size may act as an energetic barrier to ions, however, with shorter pore-pore distances (i.e., aligned nanopores) allowing for a smaller transport barrier than large pore-pore distances (i.e., misaligned nanpores) which suggested novel approach toward optimizing multilayer RO membranes in which the offset between pores can be purposely maximized to increase salt rejection while maintaining a roughly constant water flow rate per pore. However, this approach would also result in lower pore density and lower net water flux per membrane area. Therefore layer separation and pore alignment play crucial role in determining desalination performance.

The retention (R) and adsorption (Ads.) percentage for organic dyes were determined from UV-Visible absorption spectroscopy (see Figs. 3b–d along with feed and colorless permeates of R6G and MB dyes photographs post-filtration). They exhibited high retention (>92%) for charged (MB > MV) and marginally less for uncharged (R6G) solutes with hydrated radii above 5 Å (Fig. 3b reports the analysis from feed, retentate, and permeate concentrations). Interestingly, the findings display that the retentate concentration is always larger than the feed concentration, while the adsorption percentage is ~12%, irrespective of the probe molecule species. The permeability (Fig. 2) during filtration of probe molecules is almost 90% or higher to those of clean water permeability that supports minimum adsorption. Based on these measurements, it appears that SA GO and hG membranes physically sieve molecules when the interlayer space of the graphene sheets approaches the size of the probe molecules, reported as hydrated radii (~5 Å) mentioned above. It is worth noting that the negatively charged probe molecules have marginally larger retention than the positively charged molecules suggestive of electrostatic repulsion. Overall, the retention mechanism is possibly attributed to the following: (1) direct adsorption of dye molecules, (2) physical sieving by 2D nanochannels which is controlled by channel sizes and alignment and (3) electrostatic interactions between charged dyes and negatively charge surface group, on SA GO and hG membranes. To analyze further the performance, we used pore-flow model for our multilayer nanoporous membranes and qualitatively determined the reverse osmotic pressure (Δπ; hydrostatic pressure required to stop the water flow as in normal osmosis) following proposed solution-diffusion model [42]. Fig. 4 illustrates pore-flow model and associated parameters (panel a) and summarizes the outcome for different membrane types (panel b). The applicability of this phenomenological model and other attributes mentioned above once again provided the evidence of the membranes' behavior (for example, surface activity of membranes) observed in this study.

3.4. Xylem plant (white pine or Pinus strobus) as natural filtration medium

Generally, the flow of sap in plants is driven primarily by transpiration from the leaves to the atmosphere, which creates negative pressure in the xylem. Therefore, xylem morphology evolved under competing pressures of providing minimal resistance to the sap flow, while protecting against cavitation while maintaining mechanical strength [31] has some analogy to the practical membranes studied in this work. The xylem structure comprises many small conduits that work in parallel and operate in a manner that is robust to cavitation (Figs. 5a–c). The xylem conduits in conifers are formed from single dead cells known as tracheids or several cells arranged in a single file called vessels. These parallel conduits have closed ends and are connected to adjacent conduits via ''pits'' [8] (Fig. 5c). The pits have membranes with nanoscale pores that perform the critical function. The long length of xylem vessels implies that a large thickness (a few cm) of xylem tissue will be required to achieve any filtration effect. In contrast, conifers, including softwood trees have short tracheids that would force water to flow through pit membranes even for small thicknesses of xylem tissue such as in our case (Fig. 5c). Consequently, since they offer higher resistance to flow, is likely to be the most suitable xylem for construction of a water filtration device as proposed in ref. [31]. We found that water readily flowed through the xylem. The flow rate or flux was proportional to applied pressure (Figs. 5d and e), which allowed for the determination of the hydrodynamic conductivity K following:

$$Q\ (\text{volumetric flow rate}\ \left(\text{in}\ \text{m}^3\text{s}^{-1}\right)\ =\ \text{KA}\frac{\Delta P}{l}\left(\text{m}^2\text{Pa}^{-1}\text{s}^{-1}\right) \qquad (7)$$

and flux (ϕ) in similar manner as graphene-based nanoporous membranes. The observed conductivities for water (and similarly MB dye) for three or four different filters were in the range of 2–25 × 10^{-7} m^2 Pa^{-1} s^{-1} (Figs. 5d and e). Biologists have performed similar flow rate measurements by cutting a section of a plant stem under water and applying a pressure

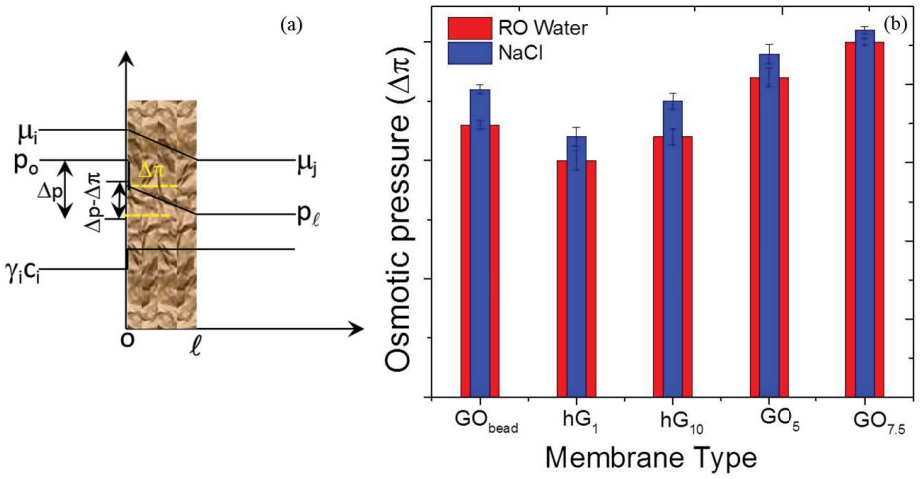

Fig. 4. (a) Chemical potential (μ), pressure (*p*) and solvent activity (*γc*) profiles in an osmotic membrane according to the pore-flow model from left to right. The concentration within the membrane is assumed to be uniform, so the chemical potential gradient in the membrane is expressed as a pressure gradient (Δ*p*). (b) Qualitative assessment of osmotic pressure (Δπ) histogram from Fig. 2 for RO water and NaCl for different membrane types.

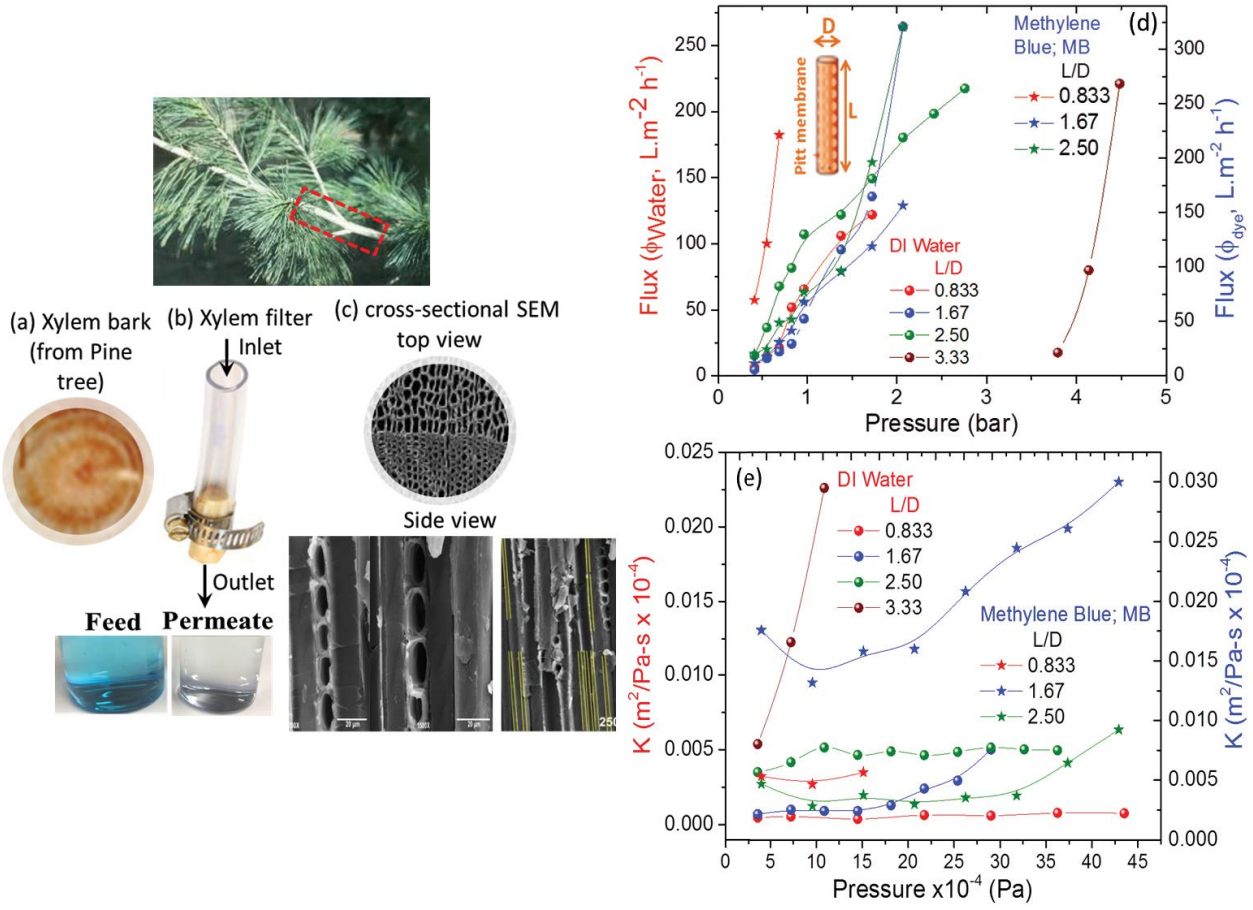

Fig. 5. (a) Photograph of a white pine tree and a clean cross-sectional pine tree (*Pinus strobus*) branch of 1.5 cm diameter, 50 μm thick after peeled off skin. (b) Xylem plant filter construct. (c) Scanning electron microscope (SEM) image of cut section showing tracheid (top view) cross section and (side view) lengthwise profile. Scale bar is 20 μm. Xylem plant filtration performance in terms of (d) flux with applied pressure (ϕ) and (e) hydrodynamic conductivity (*K*) of water and methylene blue (MB) with different aspect ratio (*L*/*D*). Hydrodynamic conductivity of the filter is deduced at each applied pressure using the total filter cross-section area and thickness. The Images of the solution before and after filtration from Xylem plant filter with *L*/*D* = 1.67 is provided.

difference to measure the flow rate [56]. Xylem conductivities of conifers typically ranged [57], which compares very well with the conductivities measured in our experiments. We also tested filters' ability to filter an organic dye with a broad particle size distribution. The blue color of the feed solution partially disappeared upon filtration (Fig. 5c) indicating that the xylem filter could effectively filter out the dye. We concluded that the flow rate measurements in our wood filter systems are consistent albeit somewhat higher with those expected from prior literature on conductivity of conifer xylem [31]. Xylem filter technology could be an attractive option for low-cost and highly efficient device for water treatment by filtration, overcoming some of the challenges associated with conventional polymeric membranes, requiring only simple replacement. The measured flow rates of about 0.1 mL s^{-1} using only a one cm^2 filter area correspond to a flow rate of over 4 L d^{-1}, sufficient to meet the drinking water requirements of one person [58].

4. Conclusion

In summary, this work was reported that the development of a large-area shear-aligned GO and hG membranes with a network of relatively aligned nanopores guided by strategic synthetic approaches and the evaluation of their performance for water detoxification (filtration and desalination). The permeance offers several fold enhancements without sacrificing the rejection rate compared with those prepared by vacuum filtered GO membranes and it is two orders of magnitude higher to those of commercial ultrafiltration membranes with similar rejection. The higher flux is attributed to the functionalized nanoporous structure, reduced channel length and controlled interlayer distance. The water flow through these organized hydrophilic nanochannels is identified as viscous while mitigating structural breakdown during relatively higher pressure driven RO process. It is demonstrated that the retention mechanism (or ion rejection and organic dyes) in membranes are co-reliant on size exclusion and/or physical sieving, electrostatic repulsion of co-ions and physio-adsorption, usually occur concurrently that affect ions rejection separations. mNPG-based membranes are promising choice as they retain many of the exceptional physicochemical properties of thin monolayer membrane and offer greater flexibility in experimental synthesis and long-term membrane production. Fabricating membranes with nanochannels through this approach is extendable to other 2D layered materials, providing potential for accelerated discoveries and innovations in the field of water purification and molecular separation.

As for xylem plant as natural filtration medium from coniferous trees, which is a mesoporous material, it is suitable as inexpensive, biodegradable and disposable system for water disinfection. However, further research and development of xylem wood filters from other genus/species could potentially lead to their widespread use, especially in developing countries.

Acknowledgments

The author (S.G.) gratefully acknowledges financial support in parts by KSEF-RDE (Grant #148-502-17-397), KY NASA EPSCoR RIDG (NASA RID-3-NNX15AK28A, subaward# 3200000029-17-229), KY NSF EPSCoR REG (subaward# 323200000271-18-059), KY NSF EPSCoR RSP (subaward# 3200000271-17-212), NSF-MRI (Grant# 1429563), and NSF EPSCoR Track RII (subaward# EPS-0814194). The student co-authors (A.H., B.E.) are thankful to KY NSF EPSCoR RSP (subaward# 3200000271-17-212) for fellowship and John Andersland (Biology) for SEM and TEM training. Finally, we would like to thank the referees for careful reading of this manuscript.

References

[1] F. Perreault, A.F. de Faria, M. Elimelech, Environmental applications of graphene-based nanomaterials, Chem. Soc. Rev., 44 (2015) 5861–5896.
[2] D. Cohen-Tanugi, J.C. Grossman, Mechanical strength of nanoporous graphene as a desalination membrane, Nano Lett., 14 (2014) 6171–6178.
[3] L.F. Greenlee, D.F. Lawler, B.D. Freeman, B. Marrot, P. Moulin, Reverse osmosis desalination: water sources, technology, and today's challenges, Water Res., 43 (2009) 2317–2348.
[4] M.A. Shannon, P.W. Bohn, M. Elimelech, J.G. Georgiadis, B.J. Mariñas, A.M. Mayes, Science and technology for water purification in the coming decades, Nature, 452 (2008) 301-310.
[5] L. Huang, M. Zhang, C. Li, G. Shi, Graphene-based membranes for molecular separation, J. Phys. Chem. Lett., 6 (2015) 2806-2815.
[6] S.P. Surwade, S.N. Smirnov, I.V. Vlassiouk, R.R. Unocic, G.M. Veith, S. Dai, S.M. Mahurin, Water desalination using nanoporous single-layer graphene, Nature Nanotechnol., 10 (2015) 459–464.
[7] F. Yao, F. Güneş, H.Q. Ta, S.M. Lee, S.J. Chae, K.Y. Sheem, C.S. Cojocaru, S.S. Xie, Y.H. Lee, Diffusion mechanism of lithium ion through basal plane of layered graphene, J. Am. Chem. Soc., 134 (2012) 8646–8654.
[8] H.L. Wang, Y. Yang, Y. Liang, J.T. Robinson, Y. Li, A. Jackson, Y. Cui, H.J. Dai, Graphene-wrapped sulfur particles as a rechargeable lithium–sulfur battery cathode material with high capacity and cycling stability, Nano Lett., 11 (2011) 2644–2647.
[9] S. Gupta, S.B. Carrizosa, B. McDonald, J. Jasinski, N. Dimakis, Graphene-family nanomaterials assembled with cobalt oxides and cobalt nanoparticles as hybrid supercapacitive electrodes and enzymeless glucose detection platforms, J. Mater. Res., 32 (2017) 301–322.
[10] S. Gupta, R. Meek, Metal nanoparticles-grafted functionalized graphene coated with nanostructured polyaniline 'hybrid' nanocomposites as high-performance biosensors, Sens. Actuators, B, 274 (2018) 85–101.
[11] Y.X. Liu, X.C. Dong, P. Chen, Biological and chemical sensors based on graphene materials, Chem. Soc. Rev., 41 (2012) 2283–2307.
[12] M. Lozada-Hidalgo, S. Hu, O. Marshall, A. Mishchenko, A.N. Grigorenko, R.A.W. Dryfe, B. Radha, I.V. Grigorieva, A.K. Geim, Sieving hydrogen isotopes through two-dimensional crystals, Science, 351 (2016) 68–70.
[13] D. Konatham, J. Yu, T.A. Ho, A. Striolo, Simulation insights for graphene-based water desalination membranes, Langmuir, 29 (2013) 11884–11897.
[14] D. Cohen-Tanugi, L.-C. Lin, J.C. Grossman, Multilayer nanoporous graphene membranes for water desalination, Nano Lett., 16 (2016) 1027-1033.
[15] M.E. Suk, N.R. Aluru, Water transport through ultrathin graphene, J. Phys. Chem. Lett., 1 (2010) 1590–1596.
[16] D.M. Stevens, J.Y. Shu, M. Reichert, A. Roy, Next-generation nanoporous materials: progress and prospects for reverse osmosis and nanofiltration, Ind. Eng. Chem. Res., 56 (2017) 10526–10551.
[17] S. Homaeigohar, M. Elbahri, Graphene membranes for water desalination, NPG Asia Mater., 9 (2017) e427–1–e427–16.
[18] A. Nicolai, B.G. Sumpter, V. Meunier, Tunable water desalination across graphene oxide framework membranes, Phys. Chem. Chem. Phys., 16 (2014) 8646–8654.

[19] M. Heiranian, A.B. Farimani, N.R. Aluru, Water desalination with a single-layer MoS_2 nanopore, Nat. Commun., 6 (2015) 1, doi: 10.1038/ncomms9616.
[20] H.Q. Gao, Q. Shi, D. Rao, Y. Zhang, J. Su, Y. Liu, Y.H. Wang, K.M. Deng, R.F. Lu, Rational design and strain engineering of nanoporous boron nitride nanosheet membranes for water desalination, J. Phys. Chem. C, 121 (2017) 22105–22113.
[21] R.K. Joshi, P. Carbone, F.C. Wang, V.G. Kravets, Y. Su, I.V. Grigorieva, H.A. Wu, A.K. Geim, R.R. Nair, Precise and ultrafast molecular sieving through graphene oxide membranes, Science, 343 (2014) 752–754.
[22] W. Scholz, H.P. Boehm, Untersuchungen am Graphitoxid. VI. Betrachtungen zur Struktur des Graphitoxids, Z. Anorg. Allg. Chem., 369 (1969) 327–340.
[23] A. Lerf, H. He, M. Forster, J. Klinowski, Structure of graphite oxide revisited, J. Phys. Chem. B, 102 (1998) 4477–4482.
[24] S. Dervin, D.D. Dionysiou, S.C. Pillai, 2D nanostructures for water purification: graphene and beyond, Nanoscale, 8 (2016) 15115–15131.
[25] K. He, A.W. Robertson, C.C. Gong, C.S. Allen, Q. Xu, H. Zandbergen, J.C. Grossman, A.I. Kirkland, J.H. Warner, Controlled formation of closed-edge nanopores in graphene, Nanoscale, 7 (2015) 11602–11610.
[26] Y. Lin, K.A. Watson, J.-W. Kim, D.W. Baggett, D.C. Working, J.W. Connell, Bulk preparation of holey graphene via controlled catalytic oxidation, Nanoscale, 5 (2013) 7814–7824.
[27] S.J. Heerem, C. Dekker, Graphene nanodevices for DNA sequencing, Nat. Nanotechnol., 11 (2016) 127–136.
[28] J. Zhao, X.T. Zhao, Z. Jiang, Z. Li, X.C. Fan, J. Zhu, H. Wu, Y. Su, D. Yang, F.H. Pan, J. Shi, Biomimetic and bioinspired membranes: preparation and application, Prog. Polym. Sci., 39 (2014) 1668–1720.
[29] S.H. Kim, J.S. Nham, Y.S. Jeong, C.S. Lee, S.H. Ha, H.B. Park, Y.J. Lee, Biomimetic selective ion transport through graphene oxide membranes functionalized with ion recognizing peptides, Chem. Mater., 27 (2015) 1255–1261.
[30] S. Balme, J.-M. Janot, L. Berardo, F. Henn, D. Bonhenry, S. Kraszewski, F. Picaud, C. Ramseyer, New bioinspired membrane made of a biological ion channel confined into the cylindrical nanopore of a solid-state polymer, Nano Lett., 11 (2011) 712–716.
[31] A. Akbari, P. Sheath, S.T. Martin, D.B. Shinde, M. Shaibani, P.C. Banerjee, R. Tkacz, D. Bhattacharyya, M. Majumder, Large-area graphene-based nanofiltration membranes by shear alignment of discotic nematic liquid crystals of graphene oxide, Nat. Commun., 7 (2016) 1–12.
[32] Y. Lin, Y.L. Liao, Z.F. Chen, J.W. Connell, Holey graphene: a unique structural derivative of graphene, Mater. Res. Lett., 5 (2017) 209–234.
[33] B. Dan, N. Behabtu, A. Martinez, J.S. Evans, D.V. Kosynkin, J.M. Tour, M. Pasquali, I.I. Smalyukh, Liquid crystals of aqueous, giant graphene oxide flakes, Soft Matter, 7 (2011) 11154–11159.
[34] S. Gupta, A. Irihamye, Probing the nature of electron transfer in metalloproteins on graphene-family materials as nano-biocatalytic scaffold using electrochemistry, AIP Adv., 5 (2015) 037106-1-037106-15.
[35] W.S. Hummers Jr., R.E. Offeman, Preparation of graphitic oxide, J. Am. Chem. Soc., 80 (1958) 1339–1339.
[36] D.C. Marcano, D.V. Kosynkin, J.M. Berlin, A. Sinitskii, Z.Z. Sun, A. Slesarev, L.B. Alemany, W. Lu, J.M. Tour, Improved synthesis of graphene oxide, ACS Nano, 4 (2010) 4806–4814.
[37] M.S.H. Boutilier, J. Lee, V. Chambers, V. Venkatesh, R. Karnik, Water filtration using plant xylem, PLoS One, 9 (2014), doi: 10.1371/journal.pone.0089934.
[38] M.J.A.D. Zohourian Mehr, K. Kabiri, Superabsorbent polymer materials: a review, Iran. Polym. J., 17 (2008) 451–477.
[39] S. Gupta, R. Meek, B. Evans, N. Dimakis, Graphene-based "hybrid" aerogels with carbon nanotubes: mesoporous network–functionality promoted defect density and electrochemical activity correlations, J. Appl. Phys., 124 (2018) 124304–1–124304–15.
[40] H.N. Lim, N.M. Huang, S.S. Lim, I. Harrison, C.H. Chia, Fabrication and characterization of graphene hydrogel via hydrothermal approach as a scaffold for preliminary study of cell growth, Int. J. Nanomed., 6 (2011) 1817–1823.
[41] X. Xie, J. Bahnemann, S. Wang, Y. Yang, M.R. Hoffmann, "Nanofiltration" enabled by super-absorbent polymer beads for concentrating microorganisms in water samples, Sci. Rep., 6 (2016) 1-8, doi: 10.1038/srep20516.
[42] R. Tkacz, R. Oldenbourg, S.B. Mehta, M. Miansari, A. Verma, M. Majumder, pH dependent isotropic to nematic phase transitions in graphene oxide dispersions reveal droplet liquid crystalline phases, Chem. Commun., 50 (2014) 6668–6671.
[43] B. Dan, G.C. Irvin, M. Pasquali, Continuous and scalable fabrication of transparent conducting carbon nanotube films, ACS Nano, 3 (2009) 835–843.
[44] J.G. Wijmans, R.W. Baker, The solution-diffusion model: a review, J. Membr. Sci., 107 (1995) 1–21.
[45] B.J. Kirby, Micro- and Nanoscale Fluid Mechanics: Transport in Microfluidic Devices, Cambridge University Press, Cambridge, UK, 2010, ISBN 978-0-521-11903-0.
[46] M. Majumder, N. Chopra, B.J. Hinds, Mass transport through carbon nanotube membranes in three different regimes: ionic diffusion and gas and liquid flow, ACS Nano, 5 (2011) 3867–3877.
[47] W.R. Bowen, J.S. Welfoot, Modelling the performance of membrane nanofiltration—critical assessment and model development, Chem. Eng. Sci., 57 (2002) 1121–1137.
[48] J. Sunner, K. Nishizawa, P. Kebarle, Ion-solvent molecule interactions in the gas phase. The potassium ion and benzene, J. Phys. Chem., 85 (1981) 1814–1820.
[49] G.S. Shi, J. Liu, C.L. Wang, B. Song, Y.S. Tu, J. Hu, H.P. Fang, Ion enrichment on the hydrophobic carbon-based surface in aqueous salt solutions due to cation-π interactions, Sci. Rep., 3 (2013) 1–6.
[50] S. Gupta, J. Robertson, Ion transport and electrochemical tuning of Fermi level in single-wall carbon nanotube probed by *in situ* Raman scattering, J. Appl. Phys., 100 (2006) 083711–1–083711–9.
[51] S. Gupta, M. Hughes, A.H. Windle, J. Robertson, Charge transfer in carbon nanotube actuators investigated using *in situ* Raman spectroscopy, J. Appl. Phys., 95 (2004) 2038–2048.
[52] X.-L. Wang, T. Tsuru, M. Togoh, S.I. Nakao, S. Kimura, Evaluation of pore structure and electrical properties of nanofiltration membranes, J. Chem. Eng. Jpn., 28 (1995) 186–192.
[53] F.G. Donnan, The theory of membrane equilibria, Chem. Rev., 1 (1924) 73–90.
[54] J. Schaep, B. Van der Bruggen, C. Vandecasteele, D. Wilms, Influence of ion size and charge in nanofiltration, Sep. Purif. Technol., 14 (1998) 155–162.
[55] T. Cassagneau, J.H. Fendler, High density rechargeable lithium-ion batteries self-assembled from graphite oxide nanoplatelets and polyelectrolytes, Adv. Mater., 10 (1998) 877–881.
[56] S. Espino, H.J. Schenk, Mind the bubbles: achieving stable measurements of maximum hydraulic conductivity through woody plant samples, J. Exp. Bot., 62 (2011) 1119–1132.
[57] J.S. Sperry, Evolution of water transport and xylem structure, Int. J. Plant Sci., 164 (2003) S115–S127.
[58] B. Reed, B. Reed, How Much Water is Needed in Emergencies, World Health Organization, Water, Engineering and Development Centre, Loughborough University, Leicestershire, UK, 2011. Available at: https://www.who.int/water_sanitation_health/publications/2011/tn9_how_much_water_en.pdf. Accessed 2014 Jan 14.